scientific reports

Check for updates

OPEN

# Research on the application of unmanned aerial vehicle aeromagnetic measurement based on rubidium optical pump magnetometer

Hanqi Zhou[1], Zhongkun Qiao[1,2,3]✉, Peng Yuan[1], Yuxiang Huang[1], Liyan Zhu[1], Chuan Yang[1], Linfei Wang[3]✉, Leilei Zheng[4]✉, Yong Wang[5]✉, Bin Wu[1]✉ & Qiang Lin[6]✉

**Optical Pumped Magnetometers (OPMs) have become key instruments in the field of precision magnetic field measurement due to their high accuracy, stability, and compact design. These quantum sensors are widely applied in geophysical exploration, engineering surveying, and unexploded ordnance detection. This study presents the $M_z$-type rubidium atomic optical pumped magnetometer developed by the Quantum Precision Measurement Team at Zhejiang University of Technology, which is integrated with a custom-designed unmanned aerial vehicle (UAV) magnetic measurement platform. Under static conditions, a performance comparison experiment was conducted between the $M_z$-type rubidium atomic optically pumped magnetometer (ZAM) and a commercial QuSpin magnetometer. Additionally, a QuSpin magnetometer was mounted on one side of the UAV platform, and a self-developed magnetometer was mounted on the other side, to verify the performance of the instrument in practical applications. Experimental results show that: in static tests, the difference between the measurement data of the two sensors had a standard deviation (STD) of 0.3nT, indicating good agreement between the two sensors; in dynamic tests, variational mode decomposition was introduced to separate the geomagnetic signal from the system environmental noise, and the processed difference between the two ZAM instruments had an STD of 1.3nT. These experimental results demonstrate that the stability and accuracy of the ZAM magnetometer are comparable to those of commercial instruments. Finally, a field experiment carried out in a metal mining area of Huzhou further verified the efficiency and practicality of UAV aerial magnetic survey, highlighting its broad application prospects in mineral exploration.**

**Keywords** Rubidium optical pump magnetometer, Unmanned aerial vehicle (UAV) magnetic surveying, Variational modal decomposition (VMD)

The geomagnetic field represents one of the most fundamental geophysical properties of the Earth, its precise measurement having significant scientific and practical value in multiple disciplines including geophysical exploration, mineral resource assessment, and engineering investigations[1–5]. In recent years, magnetic surveys of unmanned aerial vehicles (UAVs) have emerged as an effective complement to traditional manned aircraft surveys. They offer clear advantages in operational flexibility, compact size, and improved safety by eliminating personnel risk[6,7]. Such systems are especially useful for acquiring high-resolution data in challenging terrain.

[1]School of Physics, Zhejiang University of Technology, Hangzhou 310023, China. [2]Institute for Frontiers and Interdisciplinary Sciences, Zhejiang University of Technology, Hangzhou 310014, China. [3]Key Laboratory of Airborne Geophysics and Remote Sensing Geology (Ministry of Nature Resources), China Aero Geophysical Survey and Remote Sensing Center for Natural Resources, Beijing 100083, China. [4]Zhejiang Institute of Geosciences, Hangzhou 310007, China. [5]Zhejiang Geological Mineral Technology Co., Ltd., Hangzhou 310007, China. [6]State Key Laboratory of Ocean Sensing & Institute of Quantum Sensing & School of Physics, Zhejiang University, Hangzhou 310007, China. ✉email: qiaozhongkun2021@zjut.edu.cn; wlfei4103@126.com; 23500325@qq.com; 814701186@qq.com; wubin@zjut.edu.cn; qlin@zju.edu.cn

In particular, multi-rotor UAVs are well suited to detailed magnetic surveys of medium-to-small areas because of their superior maneuverability, autonomous navigation, and relatively low operational costs[8]. Early aeronautical magnetometers primarily used fluxgate technology, Fluxgate magnetometers, first conceptualized by Aschenbrenner and Goubau in 1940, have long been the sensor of choice for UAV magnetic surveys due to their compact dimensions, lightweight construction, and low power requirements[9]. Between 1953 and 1954, Packard and Varian first experimentally observed the phenomenon of free precession of protons in the Earth's magnetic field[10–12]. By 1955, based on the principle underlying this phenomenon, Packard and others proposed the design of a magnetic measurement instrument and successfully developed the world's first proton magnetometer, the V-4910[13]. Starting in the 1960, optically pumped magnetometers emerged and were put into practical use, followed by rapid development. Known for their high sampling rate and high accuracy, they have been widely adopted in the field of aeromagnetic surveys.

As a type of quantum magnetometer, the optically pumped magnetometer (OPM) exhibits outstanding advantages in sensitivity and accuracy, among other aspects. Moreover, since it does not require cryogenic cooling, is portable, reliable, and can be miniaturized, it has played an important role in applications such as geophysical magnetic detection, space magnetic detection, biomagnetic detection, fundamental physics research, as well as in atomic gyroscopes and magnetic navigation[14–18].The optical pump magnetometer is based on the Zeeman splitting of gases such as helium and the atoms of alkali metals potassium, rubidium, cesium and other elements in an external magnetic field. It has been developed by using optical pump and magnetic resonance technology, and is a magnetometer with the highest precision among the mature commercial total-field magnetometers[19].Optical pump magnetometers are developing fast and several products have appeared. The sensitivity of the P-2000 optical pump magnetometer developed by the U.S. Polatomic Company is better than 0.1 pT, representing the highest level of helium optical pump magnetometer at present[20].In terms of cesium pump magnetometer, GEOMETRICS has successfully developed a miniature cesium pump magnetometer with a volume of 15 cc, a power of 2 W and a sensitivity of 1 pT/Hz$^{1/2}$ based on MEMS technology[21].Potassium optical pump magnetometers, with a sensitivity of 0.1 pT and commercially developed by GEM Systems of Canada, are used in applications such as archaeology and anti-submarine detection. Domestic research and development of magnetometers started relatively late, with the technical level lagging behind that of foreign countries. In 1965, the Changchun Institute of Geology developed China's first optically pumped magnetometer with relatively mature technology[22].In 1976, the Helium optically pumped magnetometer developed by the Remote Sensing Center of Geology and Minerals achieved a sensitivity of 1 nT/Hz$^{1/2}$.Through subsequent technical improvements, its sensitivity was enhanced by one order of magnitude. By 1995, a handheld Helium optically pumped magnetometer was successfully developed, reaching a sensitivity of 0.05 nT/Hz$^{1/2}$.With continuous product upgrades, the HC-85 high-sensitivity Helium optically pumped magnetometer, featuring an improved accuracy of 0.01 nT, was developed in 1985[23]. While cesium and helium optical pumping magnetometers have matured in aeromagnetic surveys, the $M_z$-type optical pumping magnetometer, by comparison, offers advantages such as compact size, light weight, and low power consumption. These features enable it to better meet the demands of long-endurance operations in aeromagnetic surveys using small multi-rotor UAVs, thus making it widely adopted in the field of airborne magnetic measurement[24]. The rubidium optical pump magnetometer (ZAM) developed by Zhejiang University of Technology represents a significant advancement in quantum sensor technology for UAV applications. This system combines a compact form factor with low power consumption and robust environmental tolerance while maintaining high measurement accuracy and rapid response characteristics. The present study demonstrates the practical application of the ZAM magnetometer through comprehensive aeromagnetic surveys conducted using a multirotor UAV platform. Comparative analysis with data acquired simultaneously by a commercial QuSpin magnetometer confirms the performance parity of the ZAM system with established commercial instruments, while offering advantages in size, weight, and operational flexibility for field deployment. These results validate the readiness of the ZAM magnetometer for practical applications in geophysical surveying and establish its potential to advance the state-of-the-art in UAV-based magnetic measurement systems.

## Principle of the $M_z$-type optical pump magnetometer

The operating principle of the Mz optical pump magnetometer is to utilize the Zeeman effect of alkali metal atoms to achieve magnetic field measurements by measuring the Larmor spin frequency of polarized rubidium atoms in a weak magnetic field and inversely obtaining the magnitude of the external magnetic field.The $M_z$ optical pump atom magnetometer converts external magnetic field measurements into atomic energy level jump frequency measurements by acting on $^{87}$Rb,atoms through the Zeeman splitting, optical pumping polarization, and photomagnetic resonance effects. which converts external magnetic field measurements into measurements of atomic energy level jump frequencies. The Zeeman splitting is the theoretical basis of the magnetic field measurement, under the action of the external magnetic field $B_0$,$^{87}$Rb atom base state hyperfine energy levels are further split into multiple Zeeman subenergy levels, and the jump frequency between the split energy levels (the Larmor spin frequency $\omega_0$) is directly proportional to the external magnetic field $B_0$, which satisfies the requirement of $\omega_0 = \gamma B_0$,$\gamma$ is $^{87}$Rb atomic spin-to-magnetic ratio, a constant). Activating polarization excites atoms to jump from a low-energy state Zeeman energy level to a higher energy level(e.g., $|F_g = 2, m_F = -2\rangle \rightarrow |F_e = 2, m_F = -1\rangle$)through the use of left-handed circularly polarized lasers of a wavelength corresponding to the $D_1$ line of the $^{87}$Rb atoms (794.979 nm).$m_F = -1\rangle$),and then a large number of atoms finally accumulate to the $|F_g = 2, m_F = +2\rangle$ energy state through spontaneous radiation, thus realizing the directional arrangement of atomic magnetic moments. Finally, the RF magnetic field Brf is applied perpendicular to the laser propagation direction, and when the RF frequency is equal to the Larmor spin-in frequency $\omega_0$, the polarized atoms absorb the RF energy, redistribute among the Zeeman subenergy levels (e.g., from $|F_g = 2, m_F = +2\rangle$ back to the low-energy state),and absorb the laser light again, which results

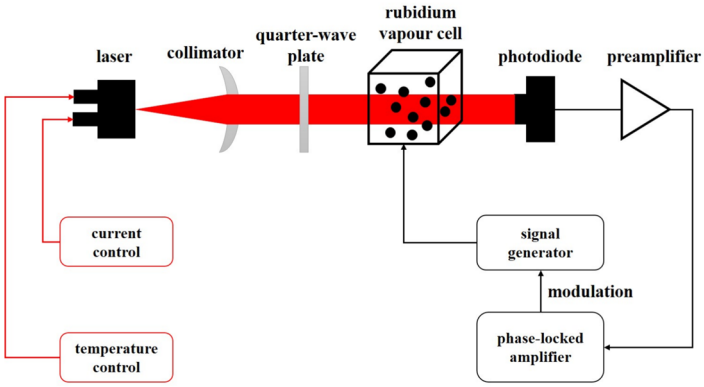


**Fig. 1**. Principle diagram of $M_z$-rubidium optical pump magnetometer.

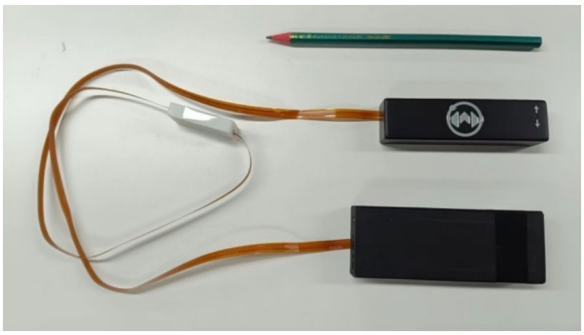

**Fig. 2**. ZAM magnetometer.

in a significant decrease in the transmitted light intensity and the formation of the photomagnetic resonance. By scanning the RF frequency to find the $\omega_0$ corresponding to the lowest point of the absorption peak, and substituting $\omega_0 = \gamma B_0$ can inversely deduce the size of the external magnetic field $B_0$, and then complete the magnetic field measurement. As shown in Fig. 1,the magnetometer system $M_z$ is as follows: first, a laser beam is collimated into parallel light, which is subsequently converted into circularly polarized light by a quarter-wave wavelength, and then injected into an atomic vapor chamber. In the vapor chamber, circularly polarized light is optically pumped to interact with rubidium atoms ($^{87}$Rb), causing the atoms to experience a population imbalance between the magnetic sub-levels. The Zeeman effect changes these energy levels proportionally with the applied magnetic field, and the resonance detection laser detects the changes in the energy levels by means of photomagnetic resonance spectroscopy. The transmitted light is collected by a photodetector, converted into an electrical signal, amplified by a low-noise preamplifier, and then processed by a lock-in amplifier for sensitive signal extraction. During the entire measurement process, an automatic current stabilization module ensures the stability of the laser output, while a precise temperature control system regulates the vapor chamber environment to ensure that the equipment is in optimal operating condition.

- *Laser Module* A vertical-cavity surface-emitting laser (VCSEL) is adopted, with an output wavelength of 795 nm and a power of 100 $\mu$W.
- *Atomic Gas Chamber* It is filled with $^{87}$Rb atoms, and the volume of the gas chamber is 5 mm$^3$.
- *Data Acquisition* Data acquisition is realized through a UART serial port, with a sampling rate of 200 Hz.
- *Probe and Circuit* The probe size is 95 mm $\times$ 25 mm $\times$ 18 mm, the circuit driving module size is 40 mm $\times$ 105 mm $\times$ 18.5 mm, and the length of the probe's flexible flat cable is about 110 cm.
- *Stabilization Power Consumption* The stable operating power consumption of the device is about 3 W.

The rubidium optical pump magnetometer (ZAM) developed by Zhejiang University of Technology is shown in Fig. 2,with detailed dimensional annotations provided in Fig. 3.

An experimental measurement was carried out on the $M_z$ magnetometer, and the obtained data are shown in Fig. 4a, with an instrument sampling rate of 200 Hz. After performing bandwidth fitting and normalization on the measured data, the calibrated noise amplitude density was obtained, as illustrated in Fig. 4b. The calibration results indicate that at 1 Hz, the sensitivity of the magnetometer is better than 3 pT, comparable to the nominal sensitivity of commercial sensors (QuSpin). (Specifically, magnetometers manufactured by QuSpin exhibit sensitivity around 3 pT/Hz$^{1/2}$, whereas those exported to China feature sensitivity as low as 20 pT/Hz$^{1/2}$.)

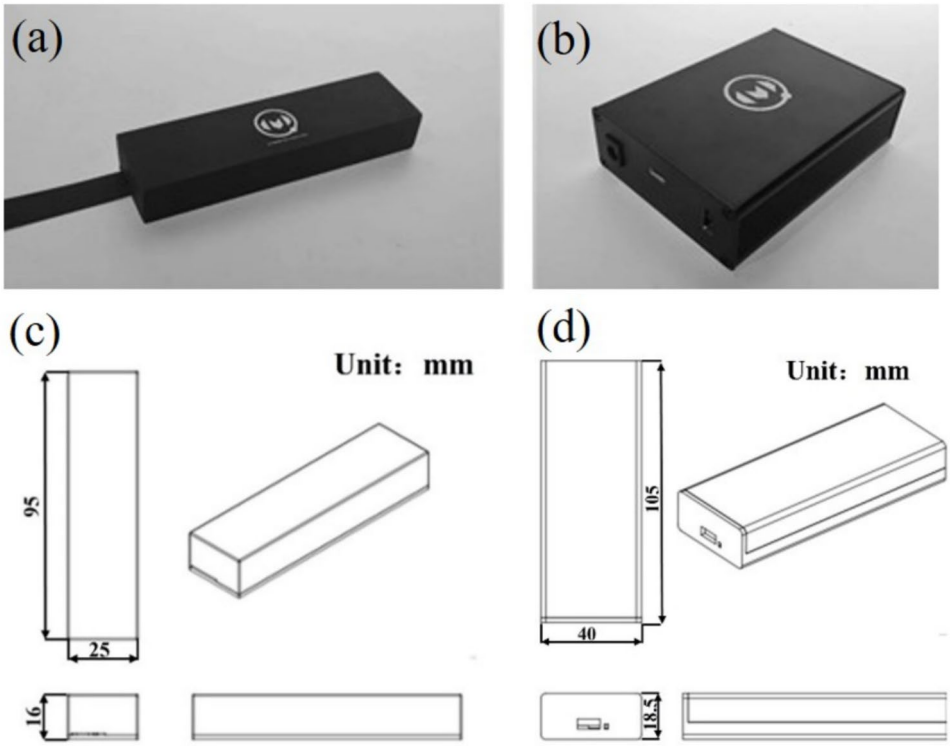


**Fig. 3**. ZAM magnetometer. (**a**) The probe structure; (**c**) Specific size of the probe; (**b**) The circuit drive modules; (**d**) Specific size of the circuit drive modules.

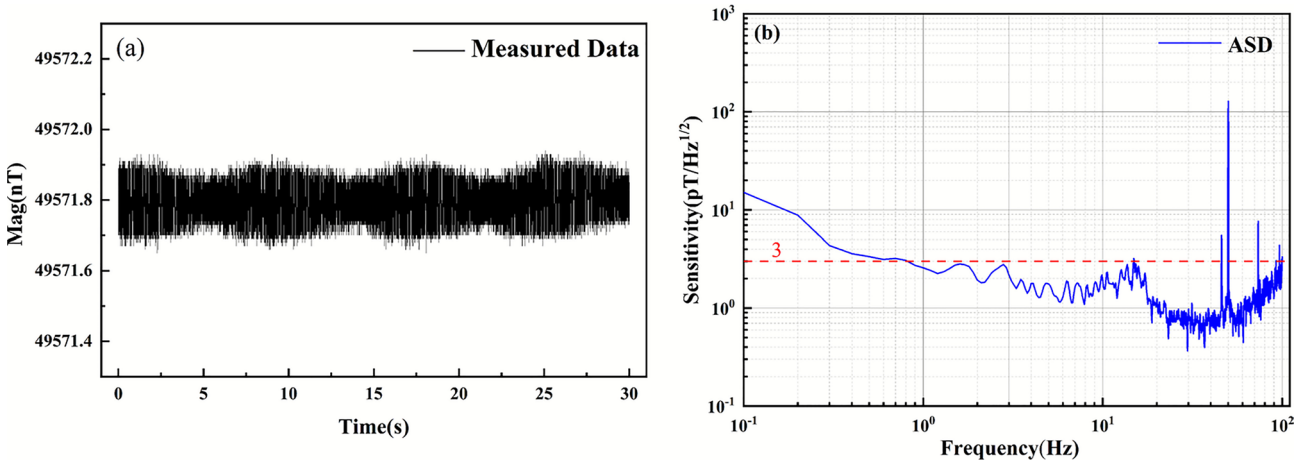


**Fig. 4**. $M_z$ magnetometer measured data and sensitivity evaluation. (**a**) Measured data; (**b**) Noise amplitude spectral density for the data in (**a**).

This research presents an integrated aeromagnetic survey system combining a rubidium optical pump magnetometer with a DJI multirotor UAV platform. The complete system architecture, illustrated in Fig. 5, incorporates several key components: an electric quadcopter drone platform that serves as the airborne carrier, a high-precision three-axis fluxgate magnetometer for reference measurements, dual optical pump magnetometers (including both the self-developed ZAM unit and a commercial QuSpin sensor for comparative analysis), and a laser altimeter for precise altitude determination. The system features fully automated operation capabilities including single-button initialization, pre-programmed flight path execution, and adaptive terrain-following functionality in complex environments, enabling acquisition of high-resolution geomagnetic anomaly data. The integrated laser altimeter provides centimeter-level elevation accuracy, significantly enhancing the spatial correlation of detected magnetic anomalies with surface geology. For performance validation, we conducted parallel measurement tests comparing the self-developed ZAM magnetometer with the reference

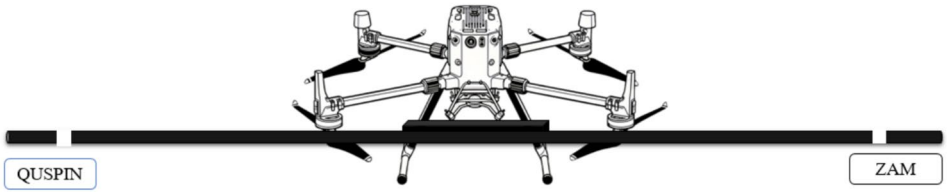


**Fig. 5**. Schematic diagram of multirotor UAV aeromagnetic system.

| UAV | ZAM | QuSpin[25] | Laser altimeter |
|---|---|---|---|
| Maximum load: 9 kg | Sensitivity: 3 pT/Hz$^{1/2}$ | Sensitivity: 20 pT/Hz$^{1/2}$ (exported to China) | Accuracy: $\leq \pm 10$ cm |
| Maximum range: 55 min | Sampling rate: 200 Hz | Sampling rate: 125/250 Hz | Weight: 77 g |
| Maximum take-off altitude: $\geq$ 7000 m | Probe weight: 30g | Probe weight: 18 g | Height measurement range: 0.5∼500 m |

**Table 1**. Technical parameters of UAV aeromagnetic system.


**Fig. 6**. Static testing experiment of QuSpin and ZAM.

QuSpin sensor. This comparative analysis evaluates key operational parameters including sensitivity, stability, and environmental adaptability under real survey conditions. The complete technical specifications of the UAV aeromagnetic system, including flight performance metrics and sensor characteristics, are systematically presented in Table 1, providing a comprehensive reference for system capabilities and operational parameters.

## Sensor performance testing

### Static testing

This static test compared the QuSpin production instrument and the quantum magnetometer sensor independently developed by the team. The test experiment is shown in Fig. 6, the blue box shows the ZAM magnetometer, while the red box shows the QuSpin. The data measured by the quantum magnetometers were processed.

Field static continuous measurements were conducted for the ZAM magnetometer and QuSpin in this study. The sampling rate of ZAM was 200 Hz, while that of QuSpin was 125 Hz. Resampling was performed on the data measured by QuSpin to increase its sampling rate to 200 Hz. Both sets of data were simultaneously processed with the same low-pass filter and had their DC components removed, using consistent filter parameters.Since the two sensors performed measurements simultaneously, they were uniformly affected by the background geomagnetic field, this effect does not interfere with the data comparison results, so diurnal variation correction was not applied. The resulting outcomes are shown in the Fig. 7, the red curve represents QuSpin, and the black curve represents ZAM. The magnetic field shape variations measured by the two instruments are consistent; the data difference ranges approximately from -1.6 to 0.8 nT, with a STD of 0.3 nT.

### Dynamic testing

We integrated two sets of ZAM magnetometers onto the wings of a drone platform to conduct dynamic aeromagnetic surveys, verifying the data stability and accuracy of ZAM under dynamic measurement conditions.

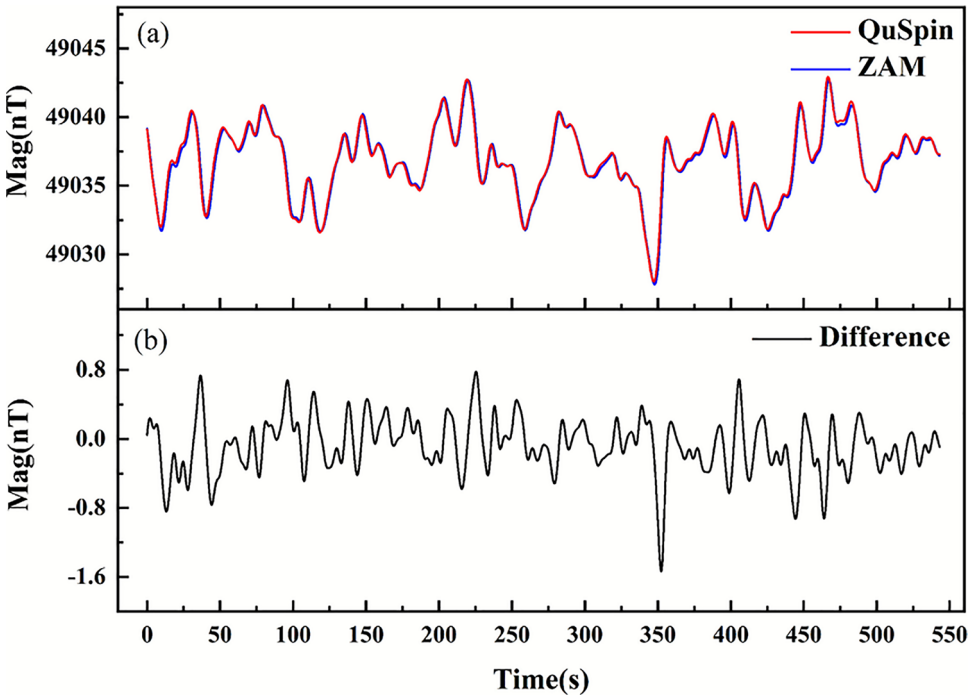


**Fig. 7**. Comparison of static test results of ZAM and QuSpin. (**a**) The test results of ZAM and QuSpin; (**b**) Difference of data.

To address carrier noise interference, we innovatively applied the VMD to separate the effective geomagnetic signal from the carrier interference noise.

*VMD*

The core idea of VMD is to construct and solve a variational problem. The VMD algorithm iteratively searches for the optimal solution of the variational model to determine the center frequency and bandwidth of each IMF, effectively separating the signal from low to high frequencies. This process involves solving the variational problem. The decomposition in VMD primarily involves Wiener filtering, the Hilbert transform, and frequency mixing. By using Wiener filtering and the Hilbert transform, the decomposition problem of original signal is converted into a variational problem of solving for $K$ modes[26,27]. To minimize the sum of the estimated bandwidths for each mode, a constrained variational model is developed, expressed as:

$$\begin{cases} \min\limits_{\{u_k\},\{\omega_k\}} \left\{ \sum\limits_{k=1}^{K} \left\| \partial_t \left[ \left( \delta(t) + \frac{j}{\pi t} \right) \cdot u_k(t) \right] e^{-j\omega_k t} \right\|_2^2 \right\} \\ s.t \sum\limits_{k=1}^{K} u_k = f(t) \end{cases} \tag{1}$$

Where $\{u_k\}$ is the set of IMF components, $\{\omega_k\}$ is the center frequency of all IMF components, $\sum\limits_k := \sum_{k=1}^{k}$ understood as the sum of all modes of components. $\left[ \left( \delta(t) + \frac{j}{\pi t} \right) * u_k(t) \right]$ is the one-sided spectrum of the resolved signal obtained by denoting $u_k(t)$ the Hilbert transform. $\left\| \partial_t \left[ \left( \delta(t) + \frac{j}{\pi t} \right) * u_k(t) \right] e^{-j\omega_k t} \right\|_2^2$ denotes the bandwidth of each IMF, estimated by calculating the square of the modulating signal gradient parameter L2. $f(t)$ denotes the input signal. In the process of solving the constructed constrained variational problem, the secondary penalty term $\beta$ and the Lagrange multiplier $\eta$ are introduced to convert the constrained problem of Eq. (1) into an unconstrained variational problem. The extended augmented Lagrange expression is given by:

$$\begin{aligned} \mathrm{L}(\{u_k\},\{\omega_k\},\eta) := \beta \sum_k \left\| \partial_t \left[ \left( \delta(t) + \frac{j}{\pi t} \right) * u_k(t) \right] e^{-j\omega_k t} \right\|_2^2 \\ + \left\| f(t) - \sum_k u_k(t) \right\|_2^2 + \left\langle \eta(t), f(t) - \sum_k u_k(t) \right\rangle \end{aligned} \tag{2}$$

The Alternating direction method of multipliers (ADMM) algorithm is used to continuously update $u_k^{n+1}$, $\omega_k^{n+1}$, and $\eta_k^{n+1}$ for each mode. The minimization problem in Eq. (1) is transformed into the 'saddle point' of Eq.

(2) after the iterative sub-optimization sequence is expanded. The expressions for the alternating optimization of $u_k$, $\omega_k$, and $\eta_k$ are:

$$u_k^{n+1}(\omega) = \frac{\hat{f}(\omega) - \sum_{i \neq k} \hat{u}_i(\omega) + \hat{\lambda}(\omega)/2}{1 + 2\beta(\omega - \omega_k)^2} \tag{3}$$

$$\hat{\omega}_k^{n+1} = \frac{\int_0^\infty \omega |\hat{u}_k(\omega)|^2 d\omega}{\int_0^\infty |\hat{u}_k(\omega)|^2 d\omega} \tag{4}$$

$$\widehat{\eta}_k^{n+1}(\omega) = \widehat{\eta}^n(\omega) + \tau \left[ \hat{f}(\omega) - \sum_k u_k^{n+1}(\omega) \right] \tag{5}$$

Where $u_k^{n+1}(\omega)$, $\hat{f}(\omega)$, and $\widehat{\eta}(\omega)$ denote the Fourier transform corresponding to $\hat{u}_k^{n+1}(t)$, $f(t)$, and $\eta(t)$, respectively. During the iterative computation, the center frequency of each component $u_k$ is estimated using the center of gravity of the power spectrum. Overall, the VMD algorithm continuously updates each mode in the frequency domain and then transforms it into the time domain using the Fourier transform.

The dynamic flight test incorporated two independently developed rubidium atomic optical pump magnetometer systems mounted on the same UAV platform for comparative performance assessment. As demonstrated in Fig. 8, the acquired flight data exhibits agreement between both sensors in terms of waveform morphology and signal amplitude characteristics. This level of conformity was maintained throughout the entire flight duration, including during maneuvers and altitude variations, indicating robust performance of both magnetometer systems under actual operational conditions. The observed consistency in dynamic measurements validates the reliability of the sensor designs and their implementation in airborne magnetic survey applications, while the conformity metric provides a quantitative benchmark for system performance evaluation.The data measured by the two sensors are presented as follows. The difference range of the raw measurement data is approximately 5 nT, with a STD of 1.75 nT. The spikes observed in the difference plot are caused by impulse noise generated when the UAV turns during flight.

Figure 9 shows the VMD analysis, which reveals different spectral characteristics in different modes. In this study, we applied VMD to the magnetic-measurement time series to identify noise sources and remove non-physical components. IMF1 demonstrates a slowly varying temporal pattern with stable amplitude and near-zero frequency components, confirming its identification as valid geomagnetic field information. In contrast, the remaining modes exhibit pronounced high-frequency oscillatory behavior, consistent with various sources of noise interference. Spectral analysis identifies two primary noise categories: (1) IMF2 , with center frequencies at 25 Hz respectively, show strong correlation with the UAV's internal clock signals and digital

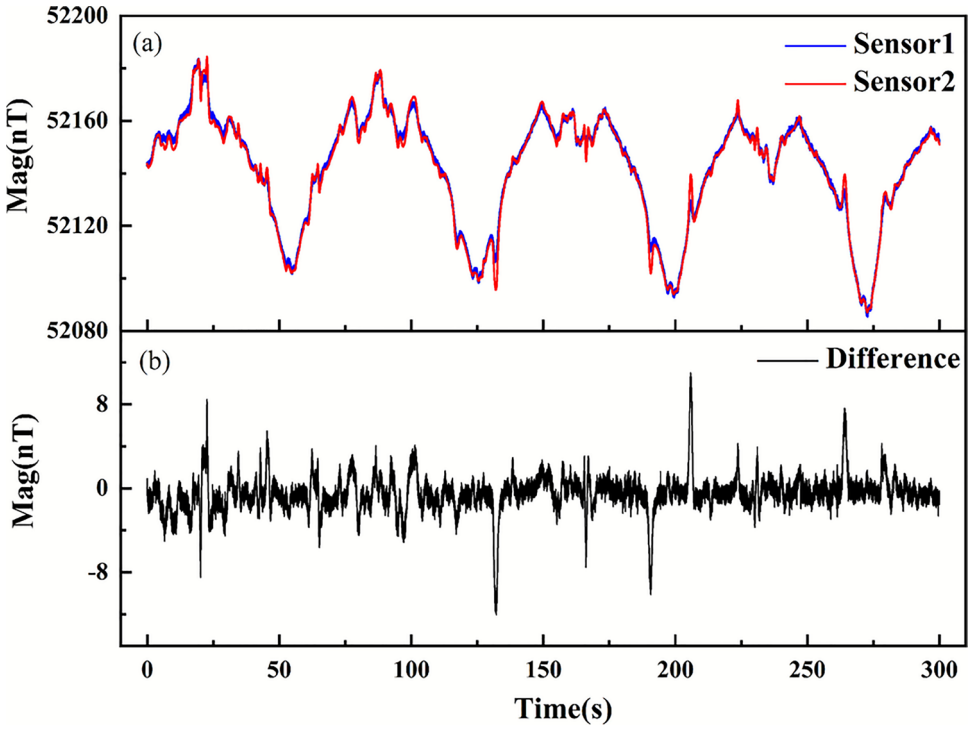


**Fig. 8**. Comparison of the original test results of two sensors. (**a**) The test results of two ZAM magnetometers flying together (original); (**b**) Difference of data.

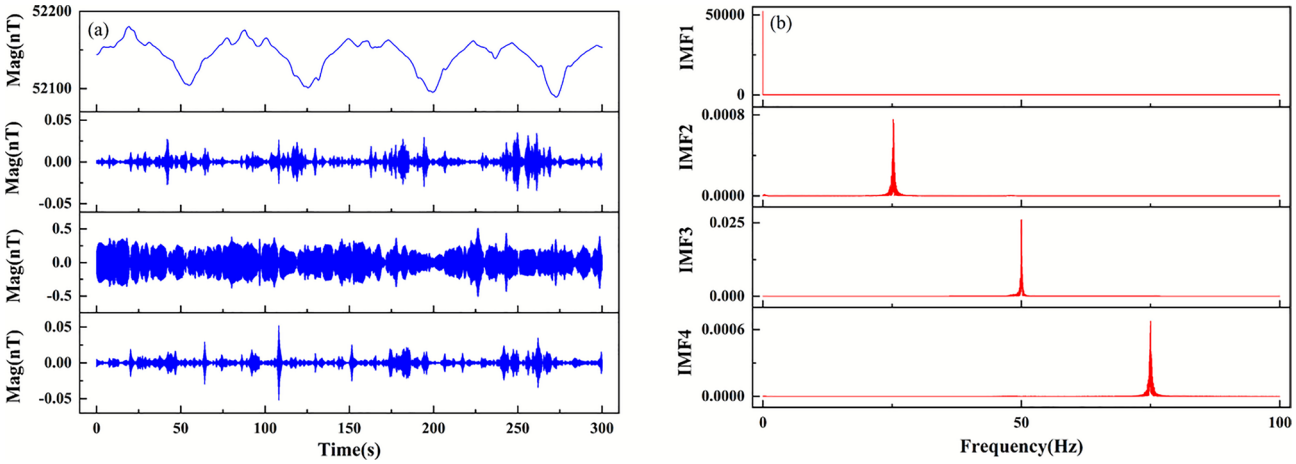


**Fig. 9**. ZAM dynamic test VMD decomposition diagram. (**a**) Time domain; (**b**) Frequency domain.

| Item (from top to bottom) | Peak-Peak (nT) | Frequency (Hz) | Signal source |
|---|---|---|---|
| IMF1 | 80 | Approaching 0 | Geomagnetic field |
| IMF2 | 0.8 | 25 | UAV onboard digital noise |
| IMF3 | 1 | 50 | Power line |
| IMF4 | 0.1 | 75 | UAV current distortion harmonics |

**Table 2**. Summary of frequency band signals of dynamic testing.

bus frequencies, suggesting electromagnetic coupling from the aircraft's electronic systems due to potential limitations in electromagnetic compatibility design; (2) IMF3, which exhibiting stable 50 Hz characteristics, clearly corresponds to power line interference.and (3) IMF4, characterized by a frequency of 75 Hz, is likely a harmonic signal generated by electromagnetic equipment onboard the UAV or resulting from current waveform distortion. The specific summary is shown in Table 2.

The reconstructed signal, as shown in the Fig. 10a and b , the data difference is approximately 3 nT, with a STD of 1.3 nT. It can be observed that noise is significantly suppressed, which indicates that the VMD method can effectively suppress noise. These results demonstrate the capability of VMD to distinguish and remove diverse noise sources while preserving geomagnetic field signatures in UAV-based magnetic surveys.

The aerial magnetic survey conducted with the ZAM magnetometer integrated on a UAV platform demonstrated promising results for geological exploration applications, while revealing several operational challenges requiring attention. Comprehensive analysis of the acquired dataset confirmed the sensor's effectiveness in detecting geomagnetic anomalies relevant to mineral exploration, with measurement accuracy meeting geological survey requirements. However, three key operational limitations were identified: (1) heading-induced measurement artifacts during flight maneuvers necessitating post-processing correction through flight-line segmentation algorithms, (2) intermittent data discontinuities (jumps) potentially caused by electromagnetic interference or sensor platform vibrations, and (3) constrained spatial coverage due to current flight endurance limitations. These observed phenomena, quantified through systematic error analysis, indicate the need for further optimization of flight protocols and sensor integration to ensure the acquisition of high-fidelity magnetic data. Subsequent investigations should focus on implementing real-time heading compensation algorithms, improving electromagnetic shielding for the sensor package, and expanding operational range through improved power management. The findings underscore both the operational viability of the ZAM magnetometer for exploration applications and the importance of addressing these technical challenges to achieve optimal survey performance under field conditions.

## Application demonstration

This study conducted a comprehensive field validation of the team's self-developed rubidium optical pump magnetometer (ZAM) against the commercial QuSpin magnetometer to assess system reliability and operational feasibility for geological prospecting applications. The experimental configuration mounted both sensors at opposite ends of a 1 m data collection pole on a quadcopter platform (Fig. 11a), enabling synchronous data acquisition under identical flight conditions. Field tests were carried out in a mineralized zone of Huzhou City, Zhejiang Province, employing an optimized S-shaped flight pattern with alternating 45° and 135° measurement lines to maintain a consistent direction of travel (Fig 11b). The survey design employs a scale of 1:10000, with adjacent survey line spacing set at 100 meters. This test flight comprised 16 parallel flight paths (including the red-marked repeat verification flight path), numbered 1 through 16 from right to left. Each individual route spans 2.4 kilometers, achieving total coverage of 38 line-kilometers across a 3.6 km² operational area. The flight

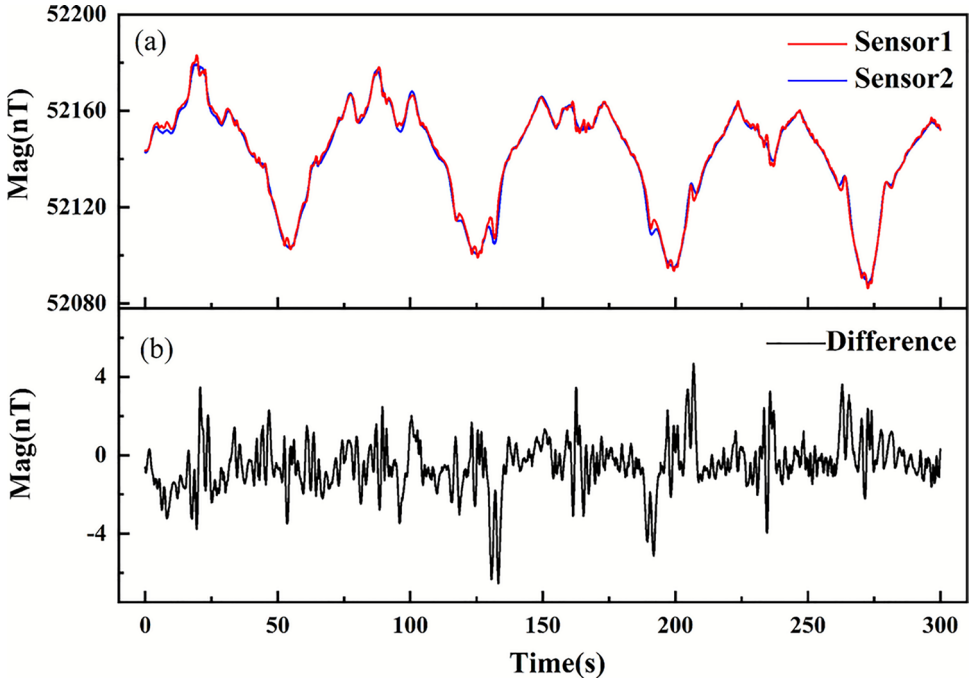


**Fig. 10**. Comparison of the test results after filtering the original data of the two sensors. (**a**) Comparison of filtered data from Sensor 1 and Sensor 2; (**b**) Difference of data.

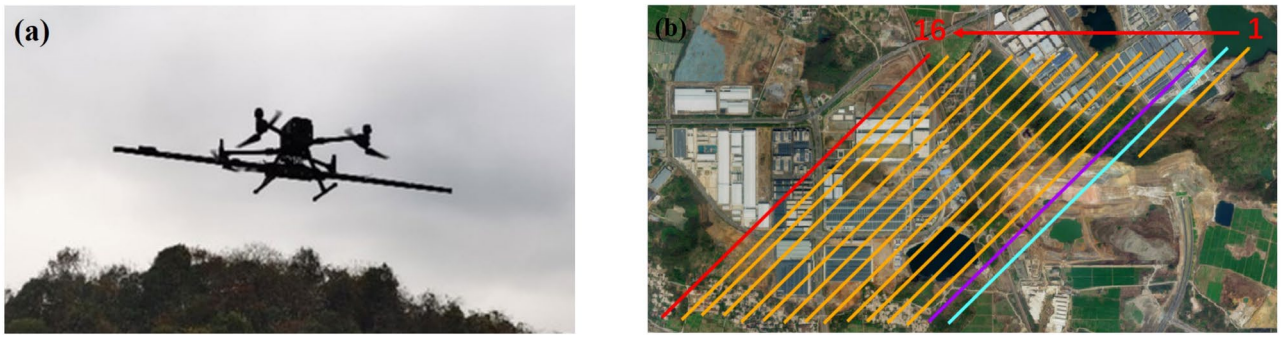


**Fig. 11**. Aeromagnetic testing site for multi-rotor UAVs. (**a**) Actual flight test diagram ( Flight altitude: 80 meters ); (**b**) Flight trajectory ( From left to right are survey lines numbered 1–16. Among them, the blue line 2 and the purple line 3 correspond to two separate external agreement assessments, while the red line 16 corresponds to an internal agreement assessment.).

parameters included a nominal speed of 10 m/s and a target altitude of 80 m, and the complete survey was carried out in four efficient flights totaling 65 minutes of effective measurement time. This configuration not only validated the consistency of the measurement between sensors, but also demonstrated the operational efficiency of UAV-based aeromagnetic systems, with the high-density flight pattern providing robust data for geological interpretation while maintaining the necessary spatial resolution for prospecting applications. The experimental design specifically addressed potential heading effects and altitude variations that could influence magnetic measurements, while the sensor spacing ensured minimal mutual interference while maintaining comparable environmental exposure conditions.

This study implemented a systematic methodology to quantitatively assess the stability and accuracy of the self-developed ZAM magnetometer through a comprehensive comparative analysis. The experimental protocol used repeated measurements along identical flight trajectories (Fig. 11, red line) to evaluate internal repeatability. Figure 12a–d present the filtered datasets from both ZAM (red) and QuSpin (black) instruments, processed using distinct filtering approaches: a custom digital low-pass filter for ZAM data versus the UAV system's integrated low-pass filter for QuSpin measurements. Comparative analysis revealed that while the ZAM data exhibited marginally higher noise levels, both datasets maintained strong consistency in both amplitude and waveform characteristics. The internal consistency evaluation of the ZAM measurements (Fig. 12d) demonstrated an accuracy of 1.21 nT, with the observed variations primarily attributable to positional deviations

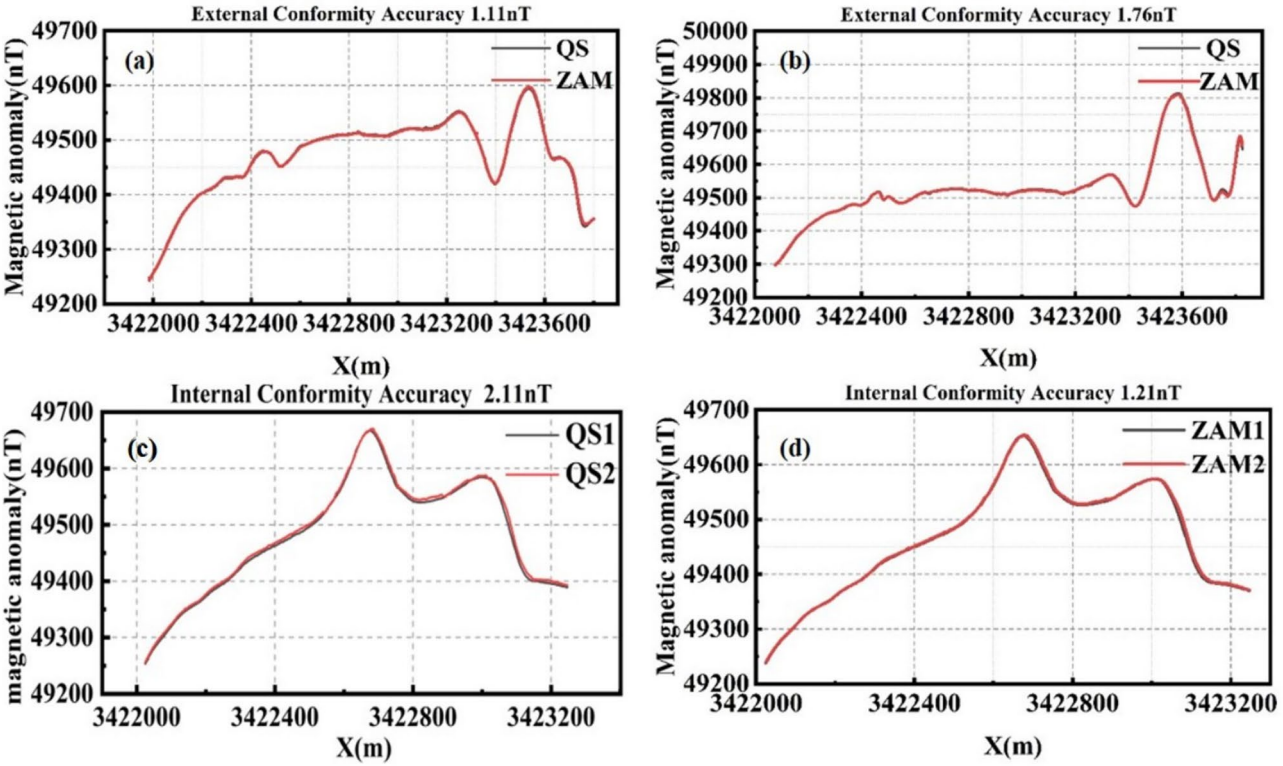


**Fig. 12**. Data comparison. (**a**) External agreement accuracy of Line 2; (**b**) External agreement accuracy of Line 3; (**c**) QuSpin internal agreement accuracy of Line 16; (**d**) ZAM internal agreement accuracy of Line 16.

| Measuring line | L2 (Qs&ZAM) | L3 (Qs&ZAM) | L16 (Qs&Qs) | L16 (ZAM&ZAM) |
|---|---|---|---|---|
| Accuracy assessment(nT) | 1.11 | 1.76 | 2.11 | 1.21 |

**Table 3**. ZAM and QuSpin accuracy table.

during reciprocal flight paths. To evaluate the consistency of measurement data from different instruments, the external coincidence accuracy for QuSpin and ZAM was calculated separately for the same flight path. The external coincidence accuracy is expressed as

$$M_{ext} = \pm\sqrt{\frac{\sum_{p=1}^{N}\left(B_{\mathrm{Qus},p} - B_{\mathrm{ZAM},p}\right)^2}{N}} \tag{6}$$

where $N$ is the number of measurement points along the survey line, $B_{\mathrm{Qus,p}}$ represents the magnetic anomaly value measured by the QUSpin instrument at point$p$, and $B_{\mathrm{ZAM,p}}$ denotes the magnetic anomaly value measured by the ZAM instrument at point $p$.

External consistency assessment between the ZAM of the research team and the commercial QuSpin sensor for identical measurement lines (Fig. 12a and b) yielded accuracy metrics ranging from 1.11 to 1.76 nT, with discrepancies mainly due to physical separation (1 m) between sensor installations. The comprehensive performance metrics across multiple flight lines, including detailed consistency measurements and comparative noise characteristics, are systematically presented in Table 3, establishing a robust quantitative framework for the evaluation of sensor performance. These results validate the measurement reliability of the self-developed magnetometer, while identifying specific areas for potential refinement in signal processing and sensor integration.

To facilitate detailed geological analysis, this study processed the raw magnetic data from both the ZAM and QuSpin instruments through a standardized preprocessing pipeline involving International Geomagnetic Reference Field (IGRF) removal, using the Minimum Curvature Gridding method to generate residual magnetic anomaly maps (Fig. 13a and b). The resultant contour maps demonstrate remarkable consistency between both sensors in terms of anomaly spatial distribution, amplitude characteristics, and morphological features. The study area exhibits a coherent north-south trending magnetic anomaly pattern, with values progressively increasing from northern latitudes (minimum values of -179.6 nT for ZAM and -181.7 nT for QuSpin) to a central maximum (378.9 nT for ZAM and 378.7 nT for QuSpin), followed by a gradual southern decrease. The

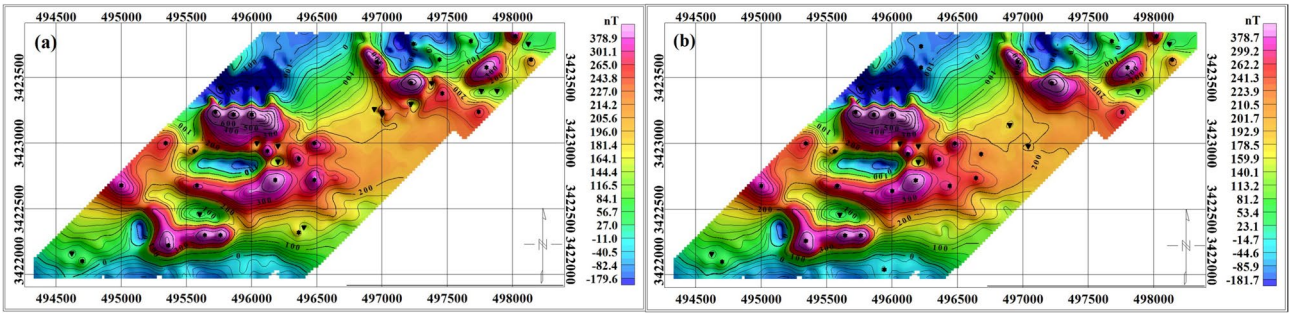


**Fig. 13**. Magnetic anomaly contour maps obtained from ZAM and QuSpin. (**a**) ZAM magnetic anomaly contour map; (**b**) QuSpin magnetic anomaly contour map.

total anomaly ranges measured 558.5 nT (ZAM) and 560.4 nT (QuSpin).This high degree of correlation between independent measurements validates both the data processing methodology and the geological significance of the observed anomalies, while demonstrating the operational reliability of the self-developed ZAM system for quantitative magnetic surveying applications. The consistent anomaly patterns provide strong evidence for the presence of subsurface basic igneous bodies with significant magnetic susceptibility contrasts relative to the surrounding geology.

## Conclusions

This study presents the successful implementation of a self-developed $M_z$-type rubidium optical pump magnetometer (type:ZAM) within a multi-rotor UAV aeromagnetic survey platform. Through comprehensive testing and verification involving comparative experiments between static ZAM and QuSpin instruments, as well as dynamic ZAM experiments comparing two sensors. The innovative application of VMD algorithm enables effective isolation and removal of various noise sources including power supply ripple, industrial frequency interference , and UAV system noise , establishing a novel approach for processing aeromagnetic data in dynamic environments. Field validation in mineral exploration demonstrates exceptional correlation between ZAM and QuSpin magnetic anomaly maps, with both systems detecting consistent anomaly patterns and spatial distributions. While the current system shows excellent operational performance, future development will focus on three key areas: (1) enhanced environmental robustness through expanded scenario testing operational range (2) further probe miniaturization and (3) improved EMI shielding for high-interference environments. These advancements position the ZAM technology as a versatile platform for diverse applications including high-resolution mineral exploration, underwater UXO detection , and archaeological surveying, marking significant progress in the engineering application of quantum sensing technology for geophysical investigations.

## Data availability

Data will be made available on request, please contact Zhong-kun Qiao at e-mail qiaozhongkun2021@zjut.edu.cn.

Received: 26 August 2025; Accepted: 30 December 2025
Published online: 09 January 2026

## References

1. Qiao, Z. et al. Research on aeromagnetic compensation of a multi-rotor uav based on robust principal component analysis. *J. Appl. Geophys.***206**, 104791. https://doi.org/10.1016/j.jappgeo.2022.104791 (2022).
2. Xiong, S. et al. Research on the development strategy of aviation geophysical exploration technology. *Chin Eng Sci***26**, 104–116. https://doi.org/10.15302/J-SSCAE-2024.05.011 (2024).
3. Døssing, A. et al. On the origin of the amerasia basin and the high arctic large igneous province: Results of new aeromagnetic data. *Earth Planet. Sci. Lett.***363**, 219–230. https://doi.org/10.1016/j.epsl.2012.12.013 (2013).
4. Michael, C., Samson, C., Wood, A. & Cook, I. Aeromagnetic surveying with a rotary-wing unmanned aircraft system: A case study from a zinc deposit in nash creek, new brunswick, canada. *Pure Appl. Geophys.***175**, 3145–3158. https://doi.org/10.1007/s00024-017-1736-2 (2017).
5. Martelet, G. et al. Airborne/uav multisensor surveys enhance the geological mapping and 3d model of a pseudo-skarn deposit in ploumanac'h, french brittany. *Minerals***11**, 1259. https://doi.org/10.3390/min11111259 (2021).
6. Qiao, Z. et al. Application of UAV aeromagnetic prospecting based on Euler deconvolution. *J Jilin Univ (Earth Sci Edit)***51, 552–560**, 10.13278/j.cnki.jjuese.20200145 (2021).
7. Qiao, Z. et al. Research on aeromagnetic three-component error compensation technology for multi-rotor uav. *J. Appl. Geophys.***193**, 102–106. https://doi.org/10.1016/j.jappgeo.2021.104406 (2021).
8. Wang, W. et al. Design and experiment of wireless power transfer systems via electromagnetic field near-zone region. *Int. J. Electron.***103**, 1736–1747. https://doi.org/10.1080/00207217.2016.1138527 (2016).
9. Wang, Y., Cheng, D., Wang, J. & Lin, J. Research on broadband differential magnetic field sensor based on nanocrystalline alloy. *Chin J Sens Actuators***9**, 1967–1970 (2007).
10. Packard, M. E. R. H. V. Free nuclear induction in the earth's magnetic field. *Phys Rev***93**, 941 (1954).
11. Waters, G. S. A measurement of the earth's magnetic field by nuclear induction. *Nature***176**(4484), 691–691 (1955).
12. Waters, G. S. & Phillips, G. A new method of measuring the earth's magnetic field. *Geophys Prospect***4**(1), 1–9 (1956).
13. L, B. A. & E., P. M.,. Magnets and magnetic field measurements. *Science***122**(3173), 738–741 (1955).

14. Alexandrov, E. B. & Bonch-Bruevich, V. A. Optically pumped atomic magnetometers after three decades. *Opt Eng* https://doi.org/10.1117/12.56132 (1992).
15. Aleksandrov, E. & Vershovskii, A. Modern radio-optical methods in quantum magnetometry. *Phys. Usp.***52**, 573–601. https://doi.org/10.3367/ufne.0179.200906f.0605 (2009).
16. Budker, D. & Romalis, M. Optical magnetometry. *Nat. Phys.***3**, 227–234. https://doi.org/10.1038/nphys566 (2007).
17. Fu, K. M., Iwata, G. Z., Wickenbrock, A. & Budker, D. Sensitive magnetometry in challenging environments. *AVS Quantum Sci***10**(1116/5), 0025186 (2020).
18. Grosz, A. et al. (eds) *High sensitivity magnetometers* Vol. 19 (Springer, Switzerland, 2017).
19. Jin, F., Yang, Y., Zheng, Z., Lu, Y. & Zhang, C. Advances in the research of atomic magnetometer. *Prog. Geophys.***26**, 1131–1136. https://doi.org/10.3969/j.issn.1004-2903.2011.03.044 (2011).
20. Kuhlman, G., Slocum, R. E. & Manning, J. P. *Battlefield applications for the polatomic 2000 magnetometer/gradiometer* (PN, 2002).
21. Accomando, F. et al. The drone-borne magnetic survey as the optimal strategy for high-resolution investigations in presence of extremely rough terrains: The case study of the Taverna San Felice quarry dike. *J. Appl. Geophys.***217**, 105186. https://doi.org/10.1016/j.jappgeo.2023.105186 (2023).
22. Zhenyu, Z. *Research on signal detection technology of helium optically pumped magnetometer*. Ph.D. thesis, Jilin University, Changchun, China (2009).
23. Yue, S. *Research on parameter optimization of helium optically pumped magnetometer and its atomic vapor cell*. Master's thesis, Harbin Engineering University, Harbin, China (2023).
24. Alexandrov, E. B. & Vershovskiy, A. K. *Mx and Mz magnetometers, chap* 4th edn. (Cambridge University Press, Cambridge, 2013).
25. Quspin.
26. Qiao, Z. et al. Research on aeromagnetic data error analysis and processing of multi-rotor uav based on variational mode decomposition algorithm. *Heliyon***8**, e11808. https://doi.org/10.1016/j.heliyon.2022.e11808 (2022).
27. Dragomiretskiy, K. & Zosso, D. Variational mode decomposition. *IEEE Trans. Signal Process.***62**, 531–544. https://doi.org/10.1109/TSP.2013.2288675 (2014).


## Acknowledgements

This paper was sponsored by National Key R&D Program of China (2023YFC2907100), the Key Laboratory of Airborne Geophysics and Remote Sensing Geology Foundation (No.2023YFL1), the Deep Earth Probe and Mineral Resources Exploration-National Science and Technology Major Project (Grant No.2024ZD1002904), and the National Natural Science Foundation of China (U24A20319). Thanks to Zhejiang University of Technology quantum precision Measurement team for providing data support.

## Author contributions

Hanqi Zhou: Performed the experiments;Analyzed and interpreted the data;Wrote the papers.Zhong-kun Qiao: Designed the experiments; Contributed re-agents, materials, analysis tools or data. Peng Yuan: Performed the experiments; Processed the dataAnalyzed. Yuxiang Huang,Liyan Zhu, Chuan Yang, Linfei Wang, Leilei Zheng, Yong Wang, Bin WU,Qiang Lin: Contributed reagents, materials, analysis tools or data.

## Funding

This article is supported by the National Key R&D Program (2023YFC2907100), the Key Laboratory of Airborne Geophysics and Remote Sensing Geology Foundation (No.2023YFL1), the Deep Earth Probe and Mineral Resources Exploration-National Science and Technology Major Project (Grant No.2024ZD1002904), and the National Natural Science Foundation of China (U24A20319).

## Declarations

## Competing interests

The authors declare no competing interests.

## Additional information

**Correspondence** and requests for materials should be addressed to Z.Q., L.W., L.Z., Y.W., B.W. or Q.L.

**Reprints and permissions information** is available at www.nature.com/reprints.

**Publisher's note** Springer Nature remains neutral with regard to jurisdictional claims in published maps and institutional affiliations.

**Open Access** This article is licensed under a Creative Commons Attribution-NonCommercial-NoDerivatives 4.0 International License, which permits any non-commercial use, sharing, distribution and reproduction in any medium or format, as long as you give appropriate credit to the original author(s) and the source, provide a link to the Creative Commons licence, and indicate if you modified the licensed material. You do not have permission under this licence to share adapted material derived from this article or parts of it. The images or other third party material in this article are included in the article's Creative Commons licence, unless indicated otherwise in a credit line to the material. If material is not included in the article's Creative Commons licence and your intended use is not permitted by statutory regulation or exceeds the permitted use, you will need to obtain permission directly from the copyright holder. To view a copy of this licence, visit http://creativecommons.org/licenses/by-nc-nd/4.0/.

© The Author(s) 2026